Electronic stacking-fault states in silicon

L. F. Mattheiss and J. R. Patel
Bell Laboratories, Murray Hill, New Jersey 07974
(Received 18 December 1980)

The nonorthogonal-tight-binding (NTB) method is applied to calculate the electronic-defect states in silicon which are produced by intrinsic, extrinsic, and twin stacking faults (ISF, ESF, and TSF, respectively) along a $\langle 111 \rangle$ axis. This NTB scheme, which utilizes a supercell geometry, includes s-p orbitals at each atomic site and contains two-center energy-overlap parameters spanning three shells of neighbors. The NTB parameters are determined by an accurate fit (rms error ≈ 0.1 eV) to the bulk silicon band structure of Chelikowsky and Cohen. These NTB results are also applied to calculate the stacking-fault energies γ; neglecting relaxation effects, this calculation yields a value for $\gamma_{\rm ISF}$ which is about twice the observed value and the relative values $\gamma_{\rm ISF} \approx \gamma_{\rm ESF} \approx 2\gamma_{\rm TSF}$. It is shown that relaxation of the perfect-crystal interlayer spacings near the fault planes reduce the corresponding γ's by about 50%, thereby bringing the calculated and observed values for $\gamma_{\rm ISF}$ into close agreement. The defect states produced by these three types of stacking faults are all qualitatively similar. They include states which are located about 0.1 eV above the valence-band maximum. However, contrary to a recent experimental study on an ESF, no fault states are found with energies below the conduction-band mimimum.

I. INTRODUCTION

In recent years, there has been an increased interest in the electronic structure of defect states in homopolar tetrahedral semiconductors such as silicon. The majority of these studies has concentrated on what can be described as bond-breaking defects. These include surfaces, vacancies, and dislocations. There have been comparatively fewer studies of defect states produced by stacking faults. These correspond to errors in the perfect-crystal stacking sequence and, at least for the lower-energy faults which are considered here, they do not involve the breaking of nearest-neighbor bonds. One therefore expects that the energies, wave functions, and charge distributions of such stacking-fault defect states would be only mildly perturbed from those of a perfect crystal, especially when compared to those produced by the bond-breaking defects.

At present, there exist relatively few experimental data on stacking-fault states in silicon. A charge collection scanning-electron-microscopy study by Kimerling *et al.*[1] on an extrinsic stacking fault in n-type silicon has provided strong evidence for the existence of defect states with energies ~0.1 eV below the conduction-band minimum. Other studies[2,3] have determined that the energy of intrinsic stacking faults in silicon $\gamma_{\rm ISF} \approx 51$–$58$ erg/cm^2.

Most theoretical studies[4,5] of stacking faults in silicon to date have been concerned with the calculation of intrinsic stacking fault energies $\gamma_{\rm ISF}$. More recently, Weigel *et al.*[6] have determined the fault energies of intrinsic, extrinsic, and twin stacking faults (hereafter denoted ISF, ESF, and TSF, respectively) using the extended Hückel theory (EHT). The only detailed study of one-electron stacking-fault states in silicon has been carried out by Louie[7] for an ESF.

The purpose of the present investigation is to determine the fault energies γ and the energy-dispersion curves $E(\vec{k})$ for ISF, ESF, and TSF states in (111) silicon. The calculations involve the nonorthogonal-tight-binding (NTB) method[8] with s-p orbitals at each silicon site and interactions extending over three shells of neighbors. The NTB parameters for this study have been determined by means of an accurate fit to the bulk empirical nonlocal-pseudopotential band structure of Chelikowsky and Cohen[9] for silicon.

The calculations utilize a hexagonal "supercell" geometry such that the stacking faults extend indefinitely in the basal plane and repeat periodically along the c axis. The supercells for the ISF, ESF, and TSF contain a total of 16, 20, and 20 atomic layers, respectively.

Although most previous tight-binding fits to the bulk silicon band structure[10-19] provide an adequate representation of the valence bands, only the most recent treatments[18,19] have succeeded in fitting the conduction bands as well. Using an NTB approach similar to the present one, del Sole and Hanke[18] obtain a fit over a 22-eV energy range with an rms error of 0.35 eV. Papaconstantopoulos and Economou,[19] assuming an orthonormal basis, obtain a slightly more accurate tight-binding fit with an rms error of about 0.30 eV. By comparison the present NTB model for silicon reproduces the bulk band structure over a more restricted energy range of 18 eV with an rms error of about 0.1 eV.

The organization of this paper is as follows. Section II contains a discussion of the stacking-

fault geometry, a review of the NTB model, and a summary of the stacking-fault energy calculations. The results of this investigation are presented in Sec. III. These include the NTB bulk silicon band structure and density of states, the calculation of stacking-fault energies, plots of the ISF, ESF, and TSF dispersion curves, and a discussion of relaxation effects.

II. DETAILS OF THE CALCULATION

A. Stacking-fault geometry

The perfect diamond lattice consists of an infinite sequence of (111) atomic planes $\ldots AA'BB'CC'AA'BB'CC'\ldots$ that are stacked in proper registry along a $\langle 111\rangle$ axis (see Fig. 1). The repeated symbols AA', etc., reflect the presence of two atoms in the primitive unit cell. The atomic positions $\vec{r}_i = \xi\vec{t}_1 + \eta\vec{t}_2 + \zeta\vec{t}_3$ can be represented in terms of a hexagonal lattice with primitive vectors

$$\vec{t}_1 = \tfrac{1}{2}a(\sqrt{3}\hat{i} - \hat{j}),\quad \vec{t}_2 = a\hat{j},\quad \vec{t}_3 = c\hat{k}, \tag{1}$$

where $a = \sqrt{2}a_0/2$ and a_0 is the cubic lattice parameter. The separation between these adjacent (111) planes is either $\sqrt{3}a_0/4$ (AA', BB', CC') or $\sqrt{3}a_0/12$ $(A'B, B'C, C'A)$ so that for n double layers, $c = \sqrt{3}na_0/3$. If one represents the perfect diamond lattice in terms of this hexagonal coordinate system, then the smallest nonprimitive unit cell corresponds to $n = 3$ and contains a total of six atoms.

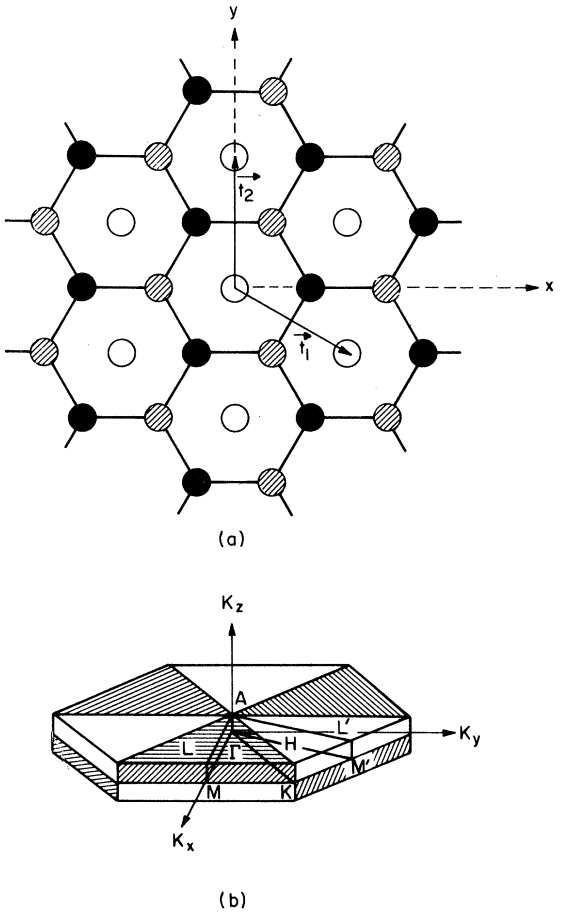

FIG. 1. (a) Projection on a (111) plane of atomic positions for AA' (unshaded), BB' (cross hatched), and CC' (shaded) type atoms. (b) Brillouin zone for the hexagonal lattice. Symmetry-related Brillouin-zone segments for the D_{3d}^3 space group are indicated.

One can readily describe the geometry of the ISF, ESF, and TSF as variations from this ideal stacking sequence. For example, the ISF is obtained by removing a pair of atomic planes (such as AA') from the ideal stacking sequence. On the other hand, an ESF is produced if one inserts, for example, a pair of BB' atomic planes between the CC' and AA' planes. Finally, the TSF is produced by imposing reflection symmetry through a plane midway between a neighboring pair such as AA'.

For investigating the electronic structure of these stacking faults, it is convenient to utilize a supercell geometry such that the stacking fault extends indefinitely in the basal plane and repeats periodically along the hexagonal c axis. This technique avoids the introduction of surfaces, whose effects would dominate and perhaps even mask the more subtle electronic effects that are due to stacking-fault defects. On the other hand, it is necessary to make the supercell sufficiently large in order to minimize the interaction between neighboring stacking faults.

As a compromise between these requirements and computational efficiency, we have chosen the supercells for the ISF, ESF, and TSF so as to include 8, 10, and 10 double layers, respectively. The space-group symmetries, lattice parameters, and atomic positions are summarized in Table I. For comparison, the corresponding results for a 9-double-layer perfect-crystal (PC) supercell are also included. From the results of this table, it is seen that the ISF is produced by removing the BB' pair $(i = 9, 10)$ from the PC cell while the ESF results from the insertion of the CC' pair $(i = 9, 10)$. In the case of the TSF, the supercell geometry requires the introduction of two fault planes between the pairs $A'A'$ $(i$ -1, 20) and CC $(i = 10, 11)$. As a result, the TSF planes are separated by only 5 double layers. The corresponding separations in the case of the ISF and ESF are 8 and 10 double layers, respectively.

As noted in Table I, the space group for the PC and TSF supercells is D_{6h}^4, whereas the ISF and ESF supercells have reduced symmetry corres-

TABLE I. Summary of space-group symmetry, lattice parameters, and atomic positions $\vec{r}_i = (\xi\vec{t}_1 + \eta\vec{t}_2 + \zeta\vec{t}_3) \equiv (\xi, \eta, \zeta)$ for the perfect crystal (PC) and ISF, ESF, and TSF supercells, respectively. $a_0 = 5.4307$ Å is the cubic lattice parameter for silicon.

	PC (D^4_{6h})		ISF (D^3_{3d})		ESF (D^3_{3d})		TSF (D^4_{6h})	
a	$\sqrt{2}a_0/2$		$\sqrt{2}a_0/2$		$\sqrt{2}a_0/2$		$\sqrt{2}a_0/2$	
c	$3\sqrt{3}a_0$		$8\sqrt{3}a_0/3$		$10\sqrt{3}a_0/3$		$10\sqrt{3}a_0/3$	
$\vec{r}_i$, i=1	(0, 0, 0)	A	(0, 0, 0)	A	(0, 0, 0)	A	(0, 0, 0)	A'
2	$(0, 0, \frac{3}{36})$	A'	$(0, 0, \frac{3}{32})$	A'	$(0, 0, \frac{3}{40})$	A'	$(\frac{1}{3}, \frac{2}{3}, \frac{1}{40})$	B
3	$(\frac{1}{3}, \frac{2}{3}, \frac{4}{36})$	B	$(\frac{1}{3}, \frac{2}{3}, \frac{4}{32})$	B	$(\frac{1}{3}, \frac{2}{3}, \frac{4}{40})$	B	$(\frac{1}{3}, \frac{2}{3}, \frac{4}{40})$	B'
4	$(\frac{1}{3}, \frac{2}{3}, \frac{7}{36})$	B'	$(\frac{1}{3}, \frac{2}{3}, \frac{7}{32})$	B'	$(\frac{1}{3}, \frac{2}{3}, \frac{7}{40})$	B'	$(\frac{2}{3}, \frac{1}{3}, \frac{5}{40})$	C
5	$(\frac{2}{3}, \frac{1}{3}, \frac{8}{36})$	C	$(\frac{2}{3}, \frac{1}{3}, \frac{8}{32})$	C	$(\frac{2}{3}, \frac{1}{3}, \frac{8}{40})$	C	$(\frac{2}{3}, \frac{1}{3}, \frac{8}{40})$	C'
6	$(\frac{2}{3}, \frac{1}{3}, \frac{11}{36})$	C'	$(\frac{2}{3}, \frac{1}{3}, \frac{11}{32})$	C'	$(\frac{2}{3}, \frac{1}{3}, \frac{11}{40})$	C'	$(0, 0, \frac{9}{40})$	A
7	$(0, 0, \frac{12}{36})$	A	$(0, 0, \frac{12}{32})$	A	$(0, 0, \frac{12}{40})$	A	$(0, 0, \frac{12}{40})$	A'
8	$(0, 0, \frac{15}{36})$	A'	$(0, 0, \frac{15}{32})$	A'	$(0, 0, \frac{15}{40})$	A'	$(\frac{1}{3}, \frac{2}{3}, \frac{13}{40})$	B
9	$(\frac{1}{3}, \frac{2}{3}, \frac{16}{36})$	B	$(\frac{2}{3}, \frac{1}{3}, \frac{16}{32})$	C	$(\frac{2}{3}, \frac{1}{3}, \frac{16}{40})$	C	$(\frac{1}{3}, \frac{2}{3}, \frac{16}{40})$	B'
10	$(\frac{1}{3}, \frac{2}{3}, \frac{19}{36})$	B'	$(\frac{2}{3}, \frac{1}{3}, \frac{19}{32})$	C'	$(\frac{2}{3}, \frac{1}{3}, \frac{19}{40})$	C'	$(\frac{2}{3}, \frac{1}{3}, \frac{17}{40})$	C
11	$(\frac{2}{3}, \frac{1}{3}, \frac{20}{36})$	C	$(0, 0, \frac{20}{32})$	A	$(\frac{1}{3}, \frac{2}{3}, \frac{20}{40})$	B	$(\frac{2}{3}, \frac{1}{3}, \frac{20}{40})$	C
12	$(\frac{2}{3}, \frac{1}{3}, \frac{23}{36})$	C'	$(0, 0, \frac{23}{32})$	A'	$(\frac{1}{3}, \frac{2}{3}, \frac{23}{40})$	B'	$(\frac{1}{3}, \frac{2}{3}, \frac{21}{40})$	B'
13	$(0, 0, \frac{24}{36})$	A	$(\frac{1}{3}, \frac{2}{3}, \frac{24}{32})$	B	$(\frac{2}{3}, \frac{1}{3}, \frac{24}{40})$	C	$(\frac{1}{3}, \frac{2}{3}, \frac{24}{40})$	B
14	$(0, 0, \frac{27}{36})$	A'	$(\frac{1}{3}, \frac{2}{3}, \frac{27}{32})$	B'	$(\frac{2}{3}, \frac{1}{3}, \frac{27}{40})$	C'	$(0, 0, \frac{25}{40})$	A'
15	$(\frac{1}{3}, \frac{2}{3}, \frac{28}{36})$	B	$(\frac{2}{3}, \frac{1}{3}, \frac{28}{32})$	C	$(0, 0, \frac{28}{40})$	A	$(0, 0, \frac{28}{40})$	A
16	$(\frac{1}{3}, \frac{2}{3}, \frac{31}{36})$	B'	$(\frac{2}{3}, \frac{1}{3}, \frac{31}{32})$	C'	$(0, 0, \frac{31}{40})$	A'	$(\frac{2}{3}, \frac{1}{3}, \frac{29}{40})$	C'
17	$(\frac{2}{3}, \frac{1}{3}, \frac{32}{36})$	C			$(\frac{1}{3}, \frac{2}{3}, \frac{32}{40})$	B	$(\frac{2}{3}, \frac{1}{3}, \frac{32}{40})$	C
18	$(\frac{2}{3}, \frac{1}{3}, \frac{35}{36})$	C'			$(\frac{1}{3}, \frac{2}{3}, \frac{35}{40})$	B'	$(\frac{1}{3}, \frac{2}{3}, \frac{33}{40})$	B'
19					$(\frac{2}{3}, \frac{1}{3}, \frac{36}{40})$	C	$(\frac{1}{3}, \frac{2}{3}, \frac{36}{40})$	B
20					$(\frac{2}{3}, \frac{1}{3}, \frac{39}{40})$	C'	$(0, 0, \frac{37}{40})$	A'

ponding to the D^3_{3d} space group. As a result, the energy bands $E(\vec{k})$ for the ISF and ESF supercell geometries have trigonal rather than full hexagonal symmetry. This is illustrated in Fig. 1(b), where the symmetry-related portions of the Brillouin zone are indicated by cross hatching. It is noted that full hexagonal symmetry is restored in the limit where the number of double layers $n \to \infty$ and the Brillouin zone becomes two dimensional.

Although the introduction of stacking faults does not alter the nearest- and second-neighbor coordination of the individual atoms from that of a perfect crystal, it does modify the number of third neighbors. The manner in which this occurs is illustrated in Fig. 2. Shown in Fig. 2(a) is a "chair"-shaped six-membered ring which is characteristic of the perfect diamond lattice. The introduction of a stacking fault transforms some of the chair-shaped rings near the fault plane to the "boat"-shaped rings of Fig. 2(b). The positions of these boat-shaped rings with respect to the fault plane is indicated by braces in Fig. 2(c) for an ISF, ESF, and TSF, respectively. Thus, a single boat-shaped ring results from a TSF, whereas the ISF's and ESF's produce pairs of such rings.

In particular, each atom in a perfect diamond lattice has 4 nearest neighbors at a distance $d_1 = \sqrt{3}a_0/4$, 12 second neighbors with $d_2 = \sqrt{2}a_0/2$, and 12 third neighbors with $d_3 = \sqrt{11}a_0/4$. For atoms at the ends of the boat-shaped rings, the number of third neighbors is reduced by 3 and these are replaced by a single neighbor at a distance $d_2' = 5\sqrt{3}a_0/12$. Since d_2' is only 2% greater than d_2, this effectively increases the number of second neighbors from 12 to 13 for these end members of boat-shaped rings.

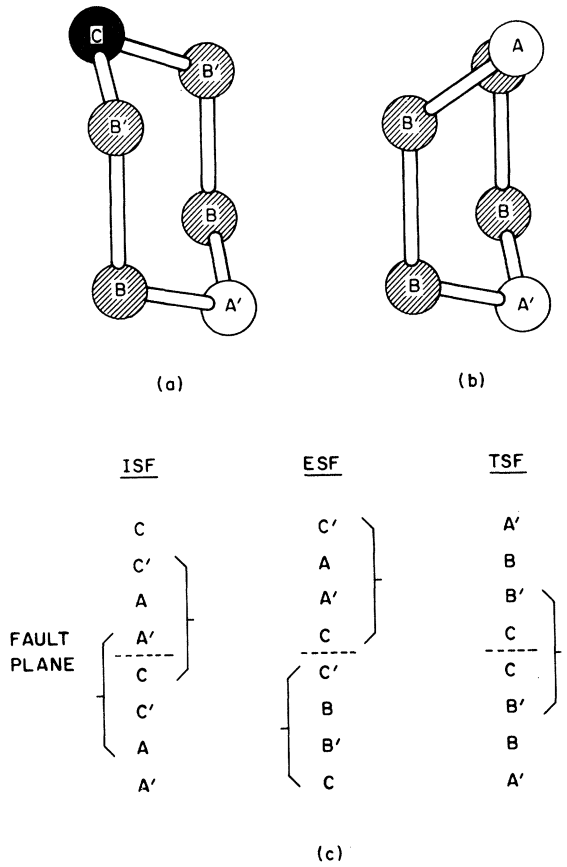

FIG. 2. (a) Chair-shaped six-membered ring which is characteristic of the perfect crystal. (b) Boat-shaped ring that occurs near stacking-fault planes, (c) Braces indicate position of boat-shaped rings with respect to fault plane in ISF, ESF, and TSF, respectively.

In the presence of a stacking fault, the long-range symmetry of the perfect diamond lattice is lost and it is no longer necessary for the spacing between adjacent atomic planes to retain their ideal values, $\sqrt{3}a_0/4$ and $\sqrt{3}a_0/12$, respectively. Relaxation effects (deviations from these ideal separations) which are symmetric with respect to the fault plane can change the lattice parameter c without altering the space-group symmetry of the ISF, ESF, and TSF supercells.

B. NTB model

The present NTB model contains s-p orbitals at each atomic site and includes energy-overlap interactions that extend over three shells of neighbors. As described previously,[8] this NTB scheme reduces the Slater-Koster[20] energy integrals $E_{\alpha,\beta}(\vec{r})$ to the two-center approximation and treats these and the corresponding overlap integrals as fitting parameters. If we denote the two-center energy integrals for the ith neighbor by $(ll'm)_i$ and the corresponding overlap integral by $[ll'm]_i$, then four energy and four overlap parameters $[(ss\sigma)_i, (sp\sigma)_i, (pp\sigma)_i, (pp\pi)_i$, etc.] are required for each shell of neighbors. Adding the orbital energies E_s and E_p, this yields a total of 26 NTB parameters.

We have determined these 26 NTB parameters for bulk silicon by means of a nonlinear least-squares fit[8] to the empirical-nonlocal-pseudopotential results of Chelikowsky and Cohen.[9] This fit was carried out at twelve points in the Brillouin zone. The band energies at these points were estimated from the published $E(\vec{k})$ curves. Since these curves included only states with energies less than 6 eV above the valence-band maximum, the remaining states with higher energies were assigned zero weight in the fitting procedure.

The resulting NTB parameters that have been obtained from this procedure are listed in Table II. The rms error for this fit is about 0.1 eV. Clearly, this error is comparable to the uncertainty with which individual energies can be extracted from the published energy-band curves.

As discussed in Sec. IIA, one effect of the introduction of a stacking fault is to change the third-neighbor coordination for atoms near the fault plane. For these atoms, the fault eliminates 3 of the 12 third neighbors ($d_3 = \sqrt{11}a_0/4$) and replaces these with a single neighbor at a distance $d_2' = 5\sqrt{3}a_0/12$ which is only 2% larger than the second-neighbor distance d_2. The corresponding two-center NTB parameters at the distance d_2' have been determined using a three-point Lagrange interpolation of the NTB parameters at the distances d_1–d_3. They are listed in parentheses in Table II.

C. Stacking-fault energies

Weigel *et al.*[6] have applied the EHT to calculate the fault energies and electron distributions of ISF, ESF, and TSF using a slab geometry. They apply the usual EHT ansatz that the total energy of the system E_{tot} is given by the sum of one-electron energies E_i weighted by the occupation numbers n_i. The fault energies γ are then obtained by subtracting E_{tot} for the perfect crystal from that of the fault structure and dividing by the cross-sectional area of the unit cell, $\sqrt{3}a^2/2$.

In their calculations, Weigel *et al.* have considered 12-layer slabs containing a PC stacking sequence, ISF, ESF, and TSF, respectively. They have averaged $E_i(\vec{k})$ over the two-dimensional Brillouin zone using six special points. One significant disadvantage of the slab geometry is that it introduces unwanted surface states in addition to

TABLE II. NTB parameters for bulk silicon. The distances d_i are in Å and the energy parameters are in eV. The values in parentheses are interpolated results for the stacking-fault calculations, as described in the text.

Orbital energies $E_s=-8.5227$ $E_p=-2.2827$						
Two-center energy parameters						
Neighbor	i	d_i	$(ss\,\sigma)_i$	$(sp\,\sigma)_i$	$(pp\,\sigma)_i$	$(pp\,\pi)_i$
	1	2.352	−3.2766	3.2668	1.9548	−1.0335
	2	3.840	−0.4515	0.7577	1.1798	−0.1535
	2′	3.919	(−0.3797)	(0.6688)	(1.0992)	(−0.1295)
	3	4.503	−0.0955	0.1523	0.3826	−0.0232
Two-center overlap parameters						
Neighbor	i	d_i	$[ss\,\sigma]_i$	$[sp\,\sigma]_i$	$[pp\,\sigma]_i$	$[pp\,\pi]_i$
	1	2.352	0.2705	−0.3426	−0.3755	0.2614
	2	3.840	0.0152	−0.0377	−0.1141	0.0140
	2′	3.919	(0.0104)	(−0.0307)	(−0.1036)	(0.0092)
	3	4.503	0.0021	−0.0077	−0.0368	−0.0001

the desired stacking-fault states. The presence of surfaces in their calculation causes, for example, their surface-layer atoms to contain five rather than four valence electrons.

As is well known, the EHT ansatz is only an approximation to the total energy since electron-electron interaction energies are counted twice and ion-ion interaction energies are omitted. The EHT assumes that these extra terms cancel in the subtraction process.

Chadi[21] has recently proposed a simplified scheme for treating these additional terms. He assumes that

$$E_{\rm tot}=E_{\rm bs}+U\ , \tag{2}$$

where $E_{\rm bs}$ is the electronic band-structure energy

$$E_{\rm bs}=\sum_{\vec{k},i} n_i(\vec{k})E_i(\vec{k})\ , \tag{3}$$

and U is the difference between the ion-ion and electron-electron interaction energies. The change in total energy $\Delta E_{\rm tot}$ is given by

$$\Delta E_{\rm tot}=\Delta E_{\rm bs}+\Delta U\ . \tag{4}$$

Chadi approximates ΔU by a short-range force-constant model of the form

$$\Delta U=\sum_{i>j}(U_1\epsilon_{ij}+U_2\epsilon_{ij}^2)\ , \tag{5}$$

where U_1 and U_2 are constants and ϵ_{ij} is the fractional change in the bond length between nearest neighbors i and j. The constant U_1 is chosen to cancel the linear term in the variation of $E_{\rm bs}$ with volume at the equilibrium separation while U_2 can be determined from the bulk modulus.

In evaluating U_1 and U_2, we have determined the distance dependence of the two-center NTB parameters using three-point Lagrange interpolation and the corresponding parameters at the equilibrium distances d_1–d_3. This procedure leads to the values $U_1=8.9$ eV and $U_2=36.2$ eV, respectively.

III. RESULTS

A. Bulk band structure

The present NTB $E(\vec{k})$ curves for silicon with a perfect diamond lattice are plotted along symmetry lines in the face-centered-cubic Brillouin zone in Fig. 3 (solid lines). For comparison, the fitted nonlocal-pseudopotential results of Chelikowsky and Cohen[9] are indicated by the filled circles. It is clear that this NTB model with interactions over three shells of neighbors provides an excellent representation of both the valence and conduction bands in silicon.

One possible discrepancy involves the conduction band with Σ_4 symmetry. It was assumed initially that this band was omitted from the plot by Chelikowsky and Cohen. Consequently, it was excluded from the NTB fitting procedure. However, the pseudopotential bands of Pickett [which are plotted in Fig. 1(b) of Ref. 19] suggest that Σ_4 and Σ_1 are very nearly degenerate along a portion of the Σ line near Γ. This suggests that the NTB Σ_4 band may be in error by ~0.5 eV.

Despite this difficulty, it is clear that the present NTB model provides a more accurate representation of the silicon conduction bands than that obtained by Papaconstantopoulos and Economou[19] using the standard Slater-Koster (SK) scheme with three shells of neighbors. Along the Δ line, the NTB model reproduces the Δ_2' maximum

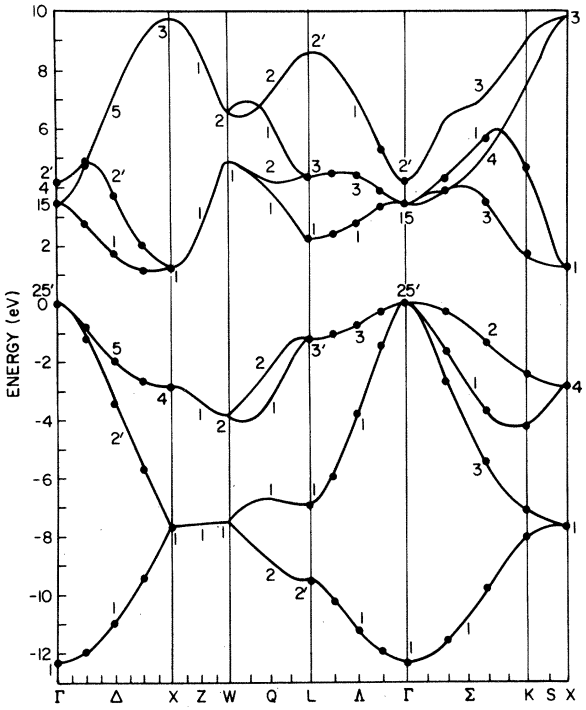

FIG. 3. NTB energy bands for silicon (solid lines). The nonlocal-pseudopotential results of Chelikowsky and Cohen (Ref. 9) are indicated by the filled circles.

whereas the SK model does not. In addition, the NTB band shapes along the Σ, Λ, and Q lines are in better accord with the pseudopotential results than those of the SK model.

In order to further check the accuracy of our NTB results, we have applied the tetrahedral method[22] to calculate an accurate density-of-states curve for silicon. These results were obtained using energy eigenvalues on a uniform cubic mesh of points with Δk equal to $\frac{1}{16}$ the ΓX line. This corresponds to 2048 tetrahedra of equal volume in $\frac{1}{48}$ of the Brillouin zone. The resulting curves are shown in Fig. 4. A comparison with the corresponding density-of-states curve of Chelikowsky and Cohen (Fig. 4 of Ref. 9) reveals excellent agreement for energies below 4 eV.

B. Stacking-fault energies

We have applied the present NTB model for silicon to calculate the ISF, ESF, and TSF energies using Eq. (4). Initially, we have neglected relaxation effects so that the nearest-neighbor bond distances are unchanged for the ISF, ESF, and TSF (see Sec. IIA). As a result, $\Delta U = 0$ according to Eq. (5). In these calculations, E_{bs} has been calculated by averaging $E_i(\vec{k})$ over six special points in the hexagonal Brillouin zone[23] for the PC and TSF and twelve points for the ISF and ESF. The

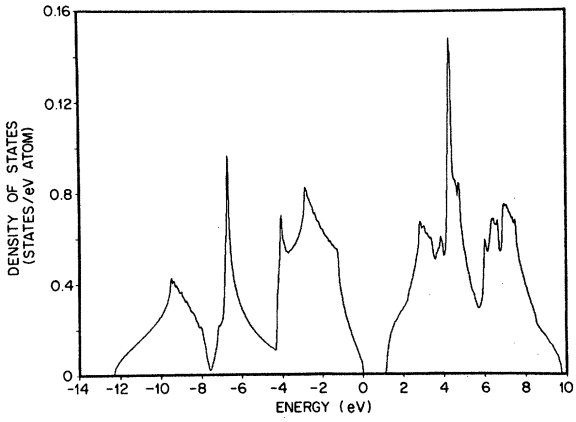

FIG. 4. NTB density-of-states curve for silicon.

six additional points are required for the latter two calculations because of the lower symmetry (D^3_{3d} vs D^4_{6h}) of the ISF and ESF space groups [see Table I and Fig. 1(b)].

Since the unit cells for the PC, ISF, ESF, and TSF contain 18, 16, 20, and 20 atoms, respectively, E_{bs} (PC) must be renormalized by the factors $\frac{8}{9}$, $\frac{10}{9}$, and $\frac{10}{9}$ before subtracting to determine the stacking-fault energy ΔE_{tot}. In particular,

$$\begin{aligned}
\Delta E_{tot}(\mathrm{ISF}) &= E_{bs}(\mathrm{ISF}) - \tfrac{8}{9}E_{bs}(\mathrm{PC}) + \Delta U\ , \\
\Delta E_{tot}(\mathrm{ESF}) &= E_{bs}(\mathrm{ESF}) - \tfrac{10}{9}E_{bs}(\mathrm{PC}) + \Delta U\ , \\
\Delta E_{tot}(\mathrm{TSF}) &= \tfrac{1}{2}[E_{bs}(\mathrm{TSF}) - \tfrac{10}{9}E_{bs}(\mathrm{PC}) + \Delta U]\ .
\end{aligned} \tag{6}$$

An extra factor of $\frac{1}{2}$ is required for ΔE_{tot}(TSF) since, as noted in Sec. IIA, the unit cell for the TSF contains two fault planes.

The results of this calculation of $\gamma = 2\Delta E_{tot}/\sqrt{3}a^2$ are summarized in Table III. We believe that the NTB results are accurate numerically to a few percent. For example, it is found that these values change (decrease) by less than 2% when the number of special points is increased by a

TABLE III. Theoretical and experimental values for the fault energies γ (in erg/cm^2). The theoretical values have been obtained using the pseudopotential (PP), extended Hückel theory (EHT), and nonorthogonal-tight-binding (NTB) methods, respectively. The arguments U and R denote unrelaxed and relaxed geometries, respectively. The latter are described in Sec. III D.

	γ_{ISF}	γ_{ESF}	γ_{TSF}	Reference
PP(U)	55			5
EHT(U)	86	85.5	43	6
NTB(U)	110	85	38	present work
NTB(R)	64	44	19	present work
Expt.	51 ± 5			2
Expt.	58 ± 6			3

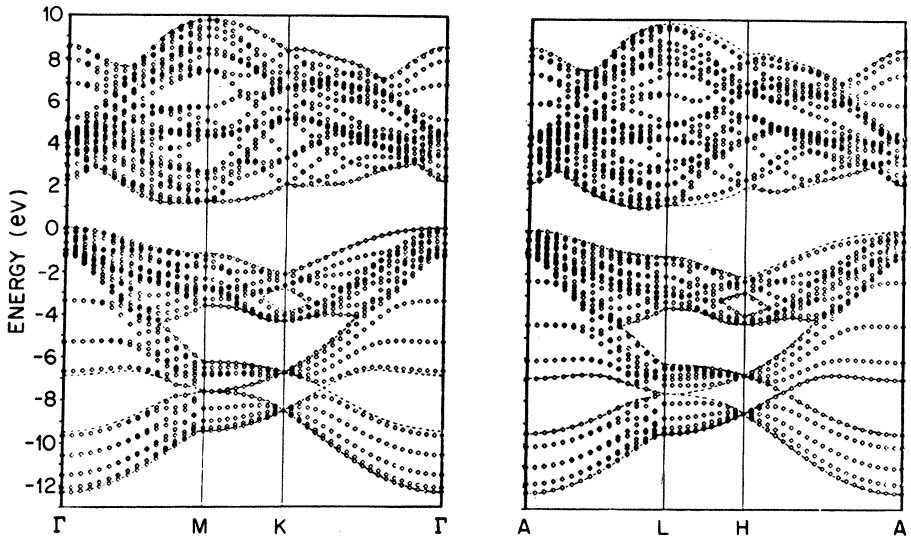

FIG. 5. Energy bands in the ΓMK and ALH planes for a silicon perfect crystal generated using a 9-double-layer supercell. The dashed lines indicate the (111) projection of the bulk band structure.

factor of 3.

For the unrelaxed geometries, the present NTB values for γ_{ISF}, γ_{ESF}, and γ_{TSF} agree quite well with the EHT results of Weigel *et al.*[6] The main difference is in the calculated value for γ_{ISF}, where the NTB value is 25% larger than the EHT result. Also, the EHT relation that $\gamma_{ISF} \approx \gamma_{ESF} \approx 2\gamma_{TSF}$ is less accurately obeyed by the NTB values.

According to the results in Table III, the unrelaxed EHT and NTB values for γ_{ISF} are substantially larger than the experimental values, whereas the pseudopotential result of Chen and Falicov[5] is in close agreement with experiment. However, as discussed in Sec. IIID, relaxation effects reduce the calculated NTB γ values by about a factor of 2, thereby reducing γ_{ISF} to the observed range of values.

In addition to calculating γ, this Brillouin-zone averaging procedure allows one to determine the electron occupation of individual layers of the hexagonal cell. In the NTB method,[8] we solve a standard secular equation involving the Hermitian matrix $S^{-1/2}HS^{-1/2}$, where H and S are the Hamiltonian and overlap matrices, respectively. The fraction of the electron density that is associated with a given layer is equal to the sum of squares of the appropriate elements in the unitary eigenvector U, averaged over the Brillouin zone.

The results of this calculation are contained in Table IV. The entries under ISF, ESF, and TSF

TABLE IV. Deviations of the valence-electron distribution $(N-4)$ (electrons/atom) for individual atom layers near ISF, ESF, and TSF planes (dashed line below and in Fig. 9). The asterisks indicate relaxed interlayer bond lengths that have been increased by +1.25% (ISF) and +0.425% (ESF and TSF), respectively.

ISF		ESF		TSF	
Unrelaxed	*Relaxed*	*Unrelaxed*	*Relaxed*	*Unrelaxed*	*Relaxed*
------	------	------	------	------	------
0.0003	0.0313*	−0.0035	−0.0025	0.0019	0.0052
0.0007	−0.0199	0.0032	0.0048*	−0.0021	0.0085*
−0.0037	−0.0069	0.0019	0.0042	−0.0011	−0.0110
0.0008	−0.0030	−0.0024	0.0076*	0.0012	−0.0011
0.0014	−0.0004	−0.0007	−0.0108	0.0001	−0.0016
0.0001	−0.0007	0.0013	−0.0009		
0.0003	−0.0001	−0.0001	−0.0012		
0.0000	−0.0002	0.0003	−0.0005		
		−0.0001	−0.0004		
		0.0000	−0.0002		

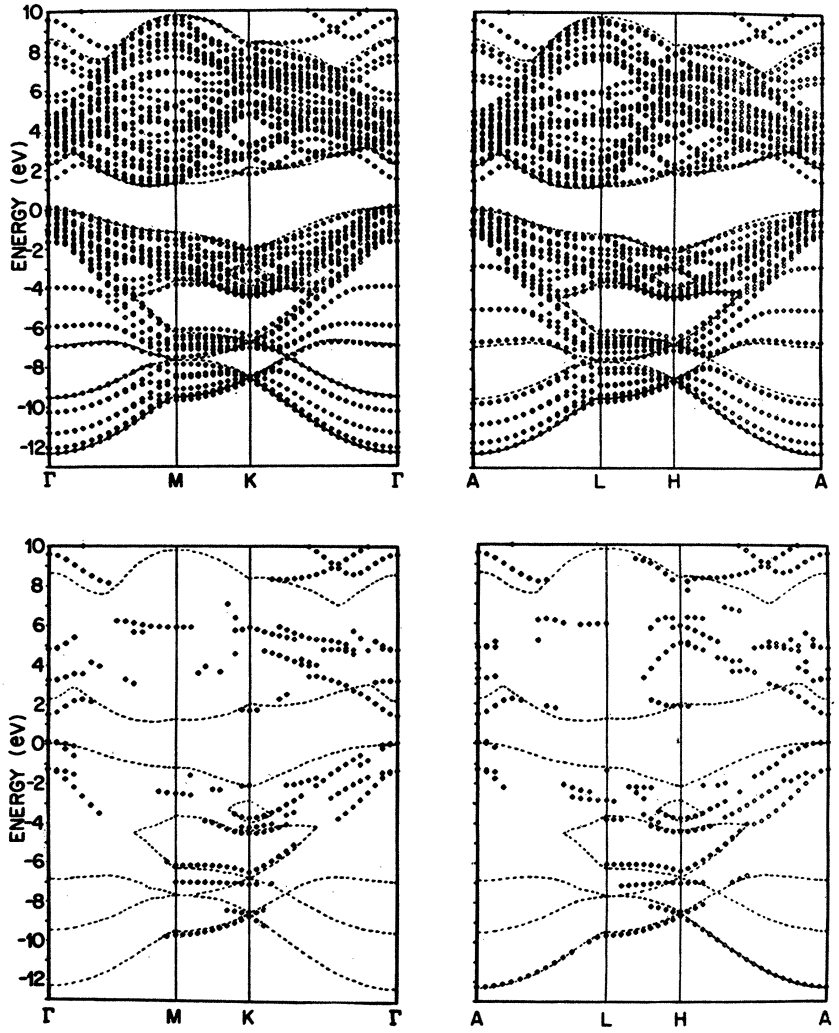

FIG. 6. Energy bands in the ΓMK and ALH planes for an 8-double-layer ISF. Shown above are the corresponding defect states for which the probability of an electron being located in the 6 layers surrounding the ISF exceeds $\frac{2}{3}$.

represent the deviations $(N-4)$ of the calculated electron distributions from the average value. Of course, these deviations are zero for the PC. It is seen that for the unrelaxed geometries, the individual layers remain essentially neutral in the presence of stacking faults. The maximum deviation corresponds to 0.1% of the average valence distribution. These deviations from neutrality are enhanced when the interlayer spacings are allowed to relax.

C. Stacking-fault states

The energy bands for PC silicon using a 9-double-layer hexagonal supercell are plotted in Fig. 5 along symmetry lines in the ΓMK and ALH planes of the Brillouin zone, respectively. The dashed lines indicate the (111) projection of the bulk NTB silicon band structure. The areas enclosed by these dashed lines would be filled by a continuum of states as the number of double layers in the unit cell were increased to infinity.

The corresponding energy-band results for the unrelaxed 8-double-layer ISF, 10-double-layer ESF, and 10-double-layer TSF supercells are plotted in the upper portions of Figs. 6–8, respectively. Shown below these are the corresponding defect states which are localized in the vicinity of the particular stacking fault. The criterion for identifying these defect states is that they possess $\frac{2}{3}$ of their electron distribution within 3 layers on either side of the ISF, 4 layers on either side of the ESF, and 2 layers on either side of the two TSF's. These layers are identified by the braces in Fig. 2(c). They include the end members of the

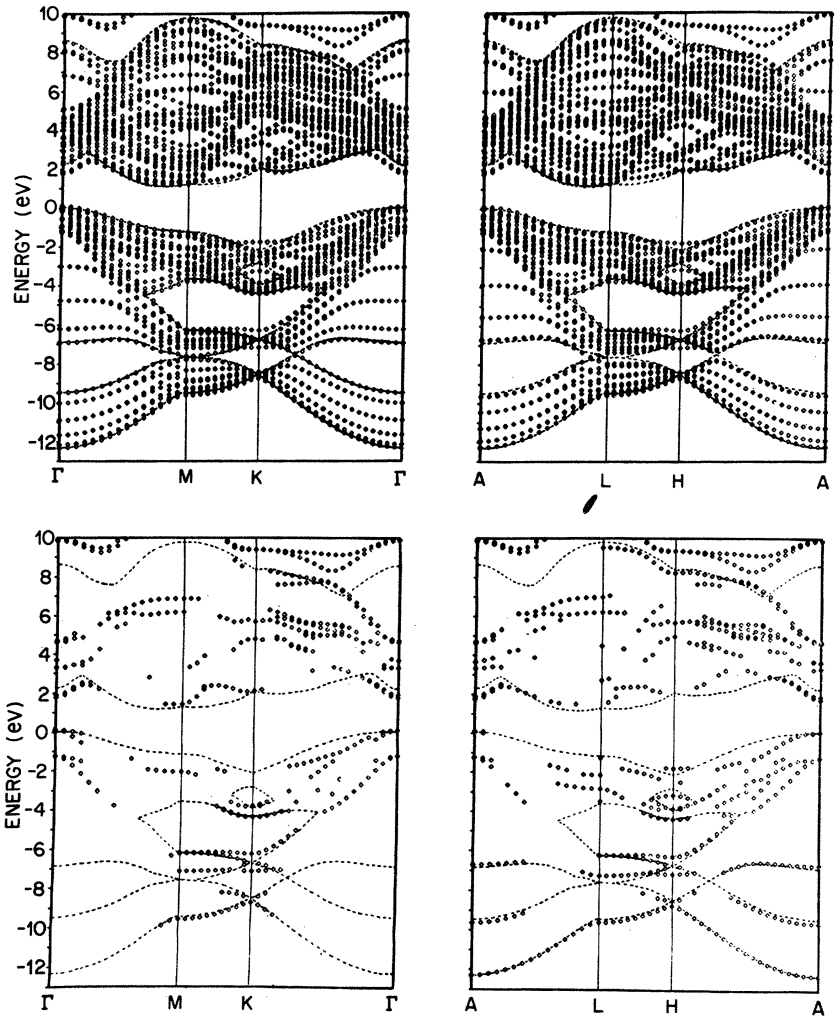

FIG. 7. Corresponding energy-band results for a 10-double-layer ESF. Defect states are $\frac{2}{3}$ localized in 8 layers surrounding ESF.

boat-shaped ring shown in Fig. 2(b).

The dashed lines in Figs. 6–8 represent the (111) projection of the bulk silicon band structure. As expected, the stacking-fault states often occur within energy gaps of the projected band structure. However, these defect states frequently continue within the energy range of the bulk band structure as defect resonances.

Qualitatively, the fault states for the ISF, ESF, and TSF are rather similar. In each case, the energy difference (dispersion) between the defect states in the ΓMK and ALH planes is a measure of the stacking-fault interaction produced by the imposition of periodic boundary conditions along the supercell c axis. Because of symmetry considerations, each defect state does not necessarily occur in both the ΓMK and ALH planes. Nevertheless, it is clear that the dispersion of the defect states along the c axis is quite negligible.

The upper portions of Figs. 6–8 contain highly localized defect states with energies well above the top of the bulk silicon conduction bands. These defect states are probably an artifact of the present NTB band model since it includes only the silicon $3s$ and $3p$ orbitals and omits all the remaining bands at higher energies.

In every case, double-degenerate defect states occur at Γ with an energy that is about 0.1 eV above the valence-band maximum. In the case of the TSF results of Fig. 8, this degeneracy is due to the presence of two faults in the TSF supercell. However, it is found that those TSF states with energies in the gap are in fact not localized in the vicinity of the fault. Instead, the localized states

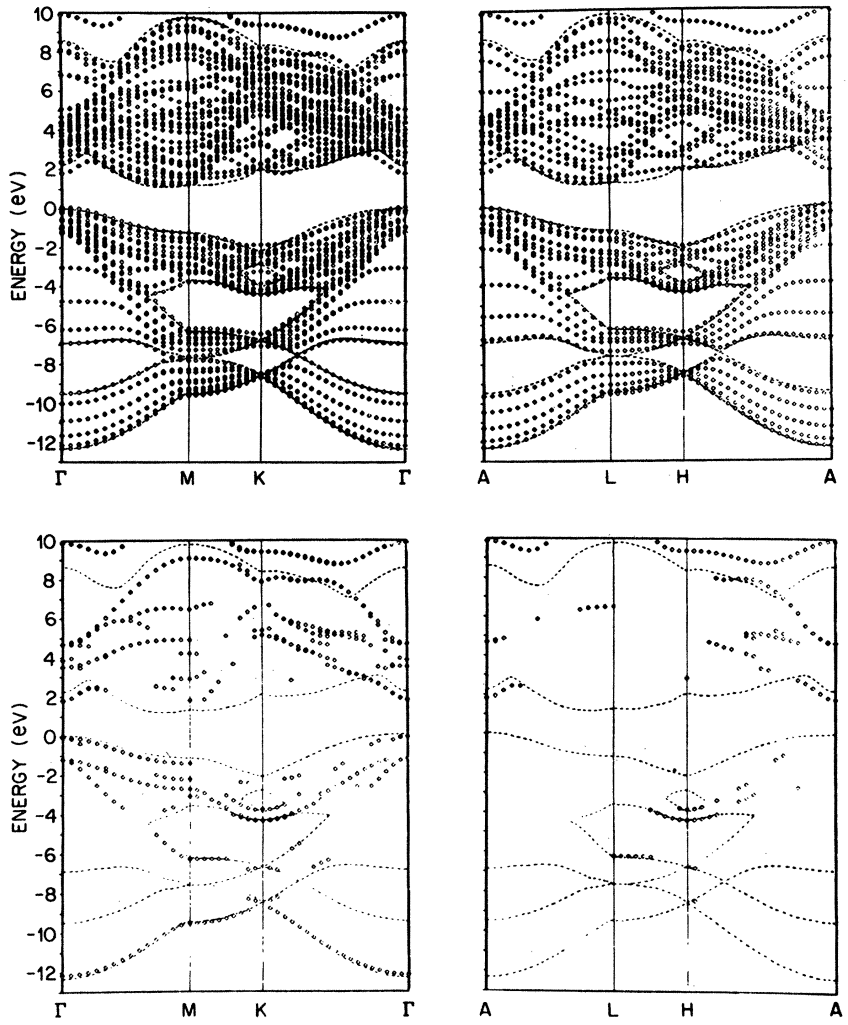

FIG. 8. Energy-band results for a pair of 5-double-layer TSF's. Defect states are $\frac{2}{3}$ localized in 4 layers surrounding each TSF.

have slightly lower energies that fall within the range of the projected band structure.

It is also found that stacking-fault states are pulled out of the conduction band at and near the zone center. This is a single band in the case of the ISF and a pair of bands for the both ESF and TSF, respectively. Although these states lie in the energy gap of the projected band structure, their energies are above that of the conduction-band minimum which occurs at 1.1 eV.

Consequently, the results of the present NTB model fail to confirm the existence of an ESF state with an energy ~0.1 eV below the conduction-band minimum that has been observed by Kimerling *et al.*[1] This suggests that the observed defect state may not be characteristic of an ideal ESF, but instead is affected by either the central precipitate or the boundary partial dislocations. Another possibility is that relaxation or reconstruction occurs in the vicinity of the stacking fault and this produces the observed ESF state. The effects of relaxation are considered in the following section.

Despite this disagreement with experiment, the calculations do predict that an analogous charge collection scanning-electron-microscopy study on ISF's, ESF's, or TSF's in p-type silicon should yield a change in signal intensity with temperature that is comparable to that observed at an ESF in n-type material.

D. Relaxation effects

In the presence of a stacking fault, ΔE_{tot} of Eq. (6) is no longer a minimum when the (111) inter-

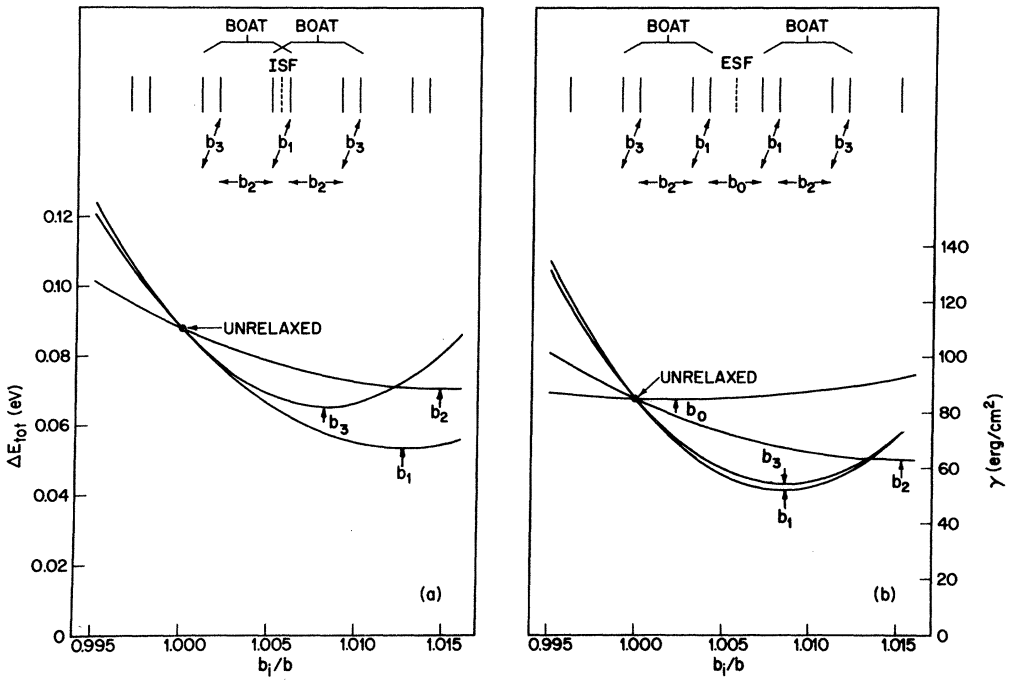

FIG. 9. Dependence of ΔE_{tot} for ISF (a) and ESF (b) on individual nearest-neighbor bond-length ratios b_i/b, where $b=\sqrt{3}a_0/4$ is the perfect-crystal value. The position of bonds relative to the fault is indicated schematically in the inset.

layer spacings are fixed at the values for the perfect silicon lattice. This leads to relaxation or deviations from these ideal separations. Because the ISF, ESF, and TSF represent a relatively weak perturbation, it is expected that these deviations will be quite small, probably about 1% of the PC nearest-neighbor bond distance. For example, Harrison[24] has shown that for aluminum, relaxation effects change the (111) layer spacings by about 1% and reduce the various fault energies by about 10%.

Ideally, one should allow each of the interlayer spacings to relax independently until a minimum value of ΔE_{tot} is obtained. Unfortunately, such a comprehensive study of relaxation effects would be awkward to carry out with the present NTB programs. As a result, we have limited the present treatment of relaxation to the first step in this procedure. Namely, we have determined the dependence ΔE_{tot} on individual bond-length variations in the vicinity of the fault planes for the ISF, ESF, and TSF supercells.

The results of this study for the ISF and ESF supercells are summarized in Figs. 9(a) and 9(b), respectively. The various curves represent ΔE_{tot} as a function of individual nearest-neighbor bond-length ratios b_i/b, where $b=\sqrt{3}a_0/4$ is the unrelaxed nearest-neighbor bond length. In determining each curve, only the specified b_i/b ratio is varied and the remaining ratios are set equal to 1. The location of the individual bonds relative to the fault plane is indicated schematically in the upper portion of the figure. It is noted that symmetry-related bonds have been varied simultaneously.

The curves are parabolas drawn through calculated values of ΔE_{tot} for bond-length ratios $b_i/b = 0.995$, 1.0, and 1.005. In every case, it is energetically favorable for the bond lengths to increase in the vicinity of the stacking fault. For the ISF, the lowest energy is obtained when $b_1 = 1.0125b$. On the other hand, both b_1 and $b_3 = 1.0085b$ yield nearly identical minima in ΔE_{tot} for the ESF. For both the ISF and ESF, this relaxation of individual bond lengths reduces ΔE_{tot} and γ by about 40%.

The systematics of these relaxation effects are more apparent when one considers the positions of the boat-shaped rings with respect to the ISF and ESF planes. These are shown in the upper portion of Fig. 9. Interlayer relaxations (such as b_0) which do not increase the separation between the end members of the boat-shaped rings have rather shallow energy minima and relaxed bond lengths which are close to the ideal value. It is found that curves similar to that shown in Fig. 9(b) for b_0 also occur for bonds involving atomic planes beyond the boat-shaped rings in both the ISF and ESF geometries.

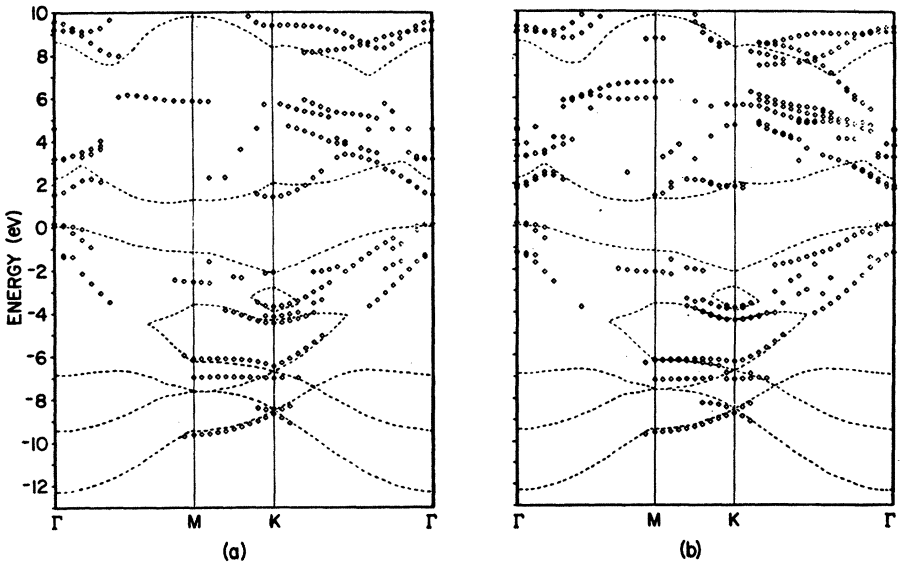

FIG. 10. Defect states for relaxed ISF (a) and ESF (b) geometries plotted as a function of wave vector in the ΓMK plane.

It is noted that the ISF and ESF curves labeled b_2 and b_3 are very similar in shape. In each case, the difference between the b_1 and b_3 curves is due to the proximity of the neighboring boat-shaped ring. This difference is small for the ESF where the rings are adjacent but significantly larger for the ISF where they overlap. It is expected that this difference between the b_1 and b_3 curves would diminish as the boat-shaped rings were moved farther apart. The two curves would coincide for the TSF geometry, where they are related by reflection symmetry.

Because of the restricted form of the allowed relaxations, the minima in Fig. 9 represent upper limits to ΔE_{tot} and the fault energies γ_{ISF} and γ_{ESF}. It is expected that a more general treatment of relaxation would further reduce ΔE_{tot} and γ by an additional 10% or so.

A calculation of γ_{ISF} for $b_1 = 1.0125b$ yields the result $\gamma_{ISF} = 64$ erg/cm^2 that is listed in Table III. The corresponding valence-electron distribution is included in the second column of Table IV. In the case of the ESF, the similarity in the b_1 and b_3 curves suggests choosing a more symmetric relaxation with $b_1 = b_3 = 1.0085b/2$. This yields $\gamma_{ESF} = 44$ erg/cm^2, which is in fact about 10% lower than the minimum in Fig. 9(b). The valence-electron distribution for this relaxed ESF geometry is contained in the fourth column of Table IV. Assuming an identical relaxation for the TSF geometry yields $\gamma_{TSF} = 19$ erg/cm^2 and the valence-electron distribution in column six of Table IV.

A survey of the results in Table IV indicates that relaxation effects tend to increase rather than decrease the deviations from neutrality of individual layers near the fault planes. In addition, they suggest that the atom layers near the fault planes tend to accumulate an excess of electrons. The ISF prediction of about 0.03 excess electrons would probably be reduced in a more general treatment of relaxation.

Finally, we consider the effect of relaxation on the ISF and ESF defect states. This is illustrated in Fig. 10 where we plot the defect states in the ΓMK plane for the relaxed ISF and ESF geometries. A comparison with the unrelaxed results shown in Figs. 6 and 7 reveals that relaxation produces few visible changes in the defect states and their dispersion. In particular, there is no indication that relaxation effects will produce defect states in the gap below the conduction-band minimum for an ESF.

Note added in proof. We have learned of a recent calculation of the electronic structure of stacking faults in silicon by Sánchez-Dehasa *et al.* using generalized Wannier functions [J. Sánchez-Dehasa, J. A. Vergés, and C. Tejedor, Phys. Rev. B 23 (in press)]. Their results are in qualitative agreement with those obtained in the present NTB study.

ACKNOWLEDGMENT

We are indebted to W. Weber for helpful discussions during the early phases of this work.

[1]L. C. Kimerling, H. J. Leamy, and J. R. Patel, Appl. Phys. Lett. 30, 217 (1977).
[2]I. L. F. Ray and D. J. H. Cockayne, Proc. R. Soc. London A325, 543 (1971).
[3]H. Alexander, J. Phys. (Paris) Suppl. 6, 7 (1979).
[4]J. Friedel, J. Less-Common Metals 28, 241 (1972).
[5]L. J. Chen and L. M. Falicov, Philos. Mag. 29, 1 (1974).
[6]C. Weigel, H. Alexander, and J. W. Corbett, Phys. Status Solidi B 71, 701 (1975).
[7]Steven G. Louie (unpublished).
[8]L. F. Mattheiss and W. Weber (unpublished).
[9]J. R. Chelikowsky and M. L. Cohen, Phys. Rev. B 10, 5095 (1974).
[10]G. Dresselhaus and M. S. Dresselhaus, Phys. Rev. 160, 649 (1967).
[11]I. Alstrup and K. Johansen, Phys. Status Solidi 28, 555 (1968).
[12]V. Bortolani, C. Calandra, and M. J. Kelly, J. Phys. C 6, L349 (1973).
[13]D. J. Chadi and M. L. Cohen, Phys. Status Solidi B 68, 405 (1975).
[14]D. J. Chadi, Phys. Rev. B 16, 790 (1977).
[15]E. Kauffer, P. Pecheur, and M. Gerl, J. Phys. C 9, 2319 (1976).
[16]K. C. Pandey and J. C. Phillips, Phys. Rev. B 13, 750 (1976).
[17]S. Froyen and W. A. Harrison, Phys. Rev. B 20, 2420 (1979).
[18]R. del Sole and W. Hanke, Solid State Commun. 31, 949 (1979).
[19]D. A. Papaconstantopoulos and E. N. Economou, Phys. Rev. B 22, 2903 (1980).
[20]J. C. Slater and G. F. Koster, Phys. Rev. 94, 1498 (1954).
[21]D. J. Chadi, Phys. Rev. B 19, 2074 (1979).
[22]O. Jepsen and O. K. Andersen, Solid State Commun. 9, 1763 (1971); G. Lehmann and M. Taut, Phys. Status Solidi B 54, 469 (1972).
[23]D. J. Chadi and M. L. Cohen, Phys. Rev. B 8, 5747 (1973).
[24]E. A. Harrison, Phys. Status Solidi A 19, 487 (1973).